

Shape-Persistent Conductive Nerve Guidance Conduits for Peripheral Nerve Regeneration

Jiahui Song, Jize Dong, Zhengchao Yuan, Moran Huang, Xiao Yu, Yue Zhao, Yihong Shen, Jinglei Wu, Mohamed EL-Newehy, Meera Moydeen Abdulhameed, Binbin Sun,* Jiwu Chen,* and Xiumei Mo*

To solve the problems of slow regeneration and mismatch of axon regeneration after peripheral nerve injury, nerve guidance conduits (NGCs) have been widely used to promote nerve regeneration. Multichannel NGCs have been widely studied to mimic the structure of natural nerve bundles. However, multichannel conduits are prone to structural instability. Thermo-responsive shape memory polymers (SMPs) can maintain a persistent initial structure over the body temperature range. Electrical stimulation (ES), utilized within nerve NGCs, serves as a biological signal to expedite damaged nerve regeneration. Here, an electrospun shape-persistent conductive NGC is designed to maintain the persistent tubular structure in the physiological temperature range and improve the conductivity. The physicochemical and biocompatibility of these P, P/G, P/G-GO, and P/G-RGO NGCs are conducted *in vitro*. Meanwhile, to evaluate biocompatibility and peripheral nerve regeneration, NGCs are implanted in subcutaneous parts of the back of rats and sciatic nerves assessed by histology and immunofluorescence analyses. The conductive NGC displays a stable structure, good biocompatibility, and promoted nerve regeneration. Collectively, the shape-persistent conductive NGC (P/G-RGO) is expected to promote peripheral nerve recovery, especially for long-gap and large-diameter nerves.

1. Introduction

The peripheral nerve is susceptible to injury caused by accidents, wars, natural disasters, and diseases, which usually further result in loss of sensory and motor functions.^[1,2] Nerve regeneration could be restored in only 50% of patients with a single nerve repair treatment, which is due to the limited ability of peripheral nerve regeneration.^[3,4] Autograft is commonly considered the “gold standard” for peripheral nerve repair, but this method still has several deficiencies, including insufficient donor sources, susceptibility of the donor site to secondary infection, and high cost.^[5] Nerve guidance conduits (NGCs) have become a promising alternative in peripheral nerve repair.^[6] Nanofiber membranes, which have the ability to mimic the structure of the extracellular matrix (ECM) with nanoscale dimensions, have been widely used in tissue engineering.^[7,8] Nowadays, thermotropic phase separation, self-assembly, and electrospinning are used to prepare nanofibers.^[9] Among, electrospinning attracts extensive attention

due to the advantages of simple operation, low investment in equipment, and a wide range of selectable processed materials.^[10] It is an effective way to make NGCs by electrospinning.

Current commercial NGCs were mainly hollow structures that were difficult to directly guide nerve regeneration and resolve axon mismatch.^[11] Multichannel structure was frequently endowed in NGCs.^[12] In addition, the topological structure can provide topographic-guided cues for nerve tissue regeneration. Aligned nanofibers altered cell behavior by guiding cell migration in a certain direction and stimulating axonal elongation.^[13] During nerve regeneration, multichannel NGCs may collapse and deform as the material degrades. Thermo-responsive shape memory polymers (SMPs) could maintain a persistent tube structure over a range of temperature changes in the body. Previous research showed that axons require a stable substrate to grow, making thermo-responsive shape memory NGCs with persistent shape an excellent candidate for long-gap and large-diameter nerve regeneration.^[14] Given these requirements, three-channel shape memory nerve conduits were designed. Poly

J. Song, Z. Yuan, X. Yu, Y. Zhao, Y. Shen, J. Wu, B. Sun, X. Mo
State Key Laboratory for Modification of Chemical Fibers and Polymer Materials
Shanghai Engineering Research Center of Nano-Biomaterials and Regenerative Medicine
College of Biological Science and Medical Engineering
Donghua University
Shanghai 201620, P. R. China
E-mail: binbin.sun@dhu.edu.cn; xmm@dhu.edu.cn

J. Dong, M. Huang, J. Chen
Department of Sports Medicine
Shanghai General Hospital Affiliated to Shanghai Jiao Tong University
Shanghai 200080, P. R. China
E-mail: jeevechen@gmail.com

M. EL-Newehy, M. M. Abdulhameed
Department of Chemistry
College of Science
King Saud University
P.O. Box 2455, Riyadh 11451, Saudi Arabia

 The ORCID identification number(s) for the author(s) of this article can be found under <https://doi.org/10.1002/adhm.202401160>

DOI: 10.1002/adhm.202401160

(lactide-co-trimethylene carbonate), as one of the thermo-responsive SMPs, exhibits good biocompatibility, biodegradability, and glass transition temperature (T_g) near human body temperature with potential applications in nerve regeneration, blood vessel regeneration, and bone tissue engineering.^[15–17] Meanwhile, PLMC could be combined with gelatin (Gel), which provides a hydrophilic environment and then promotes cell adhesion.^[18] Therefore, multichannel NGCs with aligned nanofibers were designed.

In addition to guiding axons, the construction of NGCs also needs to provide bioactive signals to promote axon extension. Bioelectric fields can be regenerated by human movement, which in turn generates and transmits electrical signals. Among, cardiomyocytes, osteoblasts, and neurons are relatively sensitive to electrical signal stimulation.^[19–21] To stimulate the intracellular electric fields of biological systems, electrical stimulation (ES) combined with electroactive biomaterials is considered as a promising approach for nerve regeneration.^[22] Thus, many conductive polymers and conductive nanoparticles, such as polyaniline (PANI), polypyrrole (PPy), Poly (3,4-ethylenedioxythiophene) (PEDOT), gold nanoparticles, graphene nanosheets, and carbon nanotubes, were utilized to obtain conductive NGCs.^[23,24] The superior mechanical properties and electrical conductivity of graphene for neural tissue have been explored.^[25] However, the poor dispersibility of pure graphene limits its application in electrospinning. Graphene oxide (GO) is an oxidized derivative of graphene, which improves dispersion in polar solvents by hydrogen bonding for better processing performance.^[26] In addition, GO must be reduced to reduced graphene oxide (RGO) to restore conductivity.^[27]

In this study, PLMC, Gel, GO, or RGO were used to construct shape-persistent conductive NGCs. The potential of these NGCs to stimulate Schwann cells proliferation, enhance PC12 cells differentiation via ES, and provide topographical cues for cell guidance was evaluated by CCK8, Transwell, and qRT-PCR. Histological and functional assessments confirmed that the conductive P/G-RGO NGC significantly promoted nerve regeneration, as indicated by muscle weight and sciatic nerve function index. Based on shape memory property, all conduits can maintain their multichannel tubular shape at 37 °C. The shape-persistent conductive NGC holds the potential to provide successful therapeutic outcomes and long-gap and large-diameter nerve regeneration.

2. Results

2.1. Characterization of P, P/G, P/G-GO, and P/G-RGO Membranes

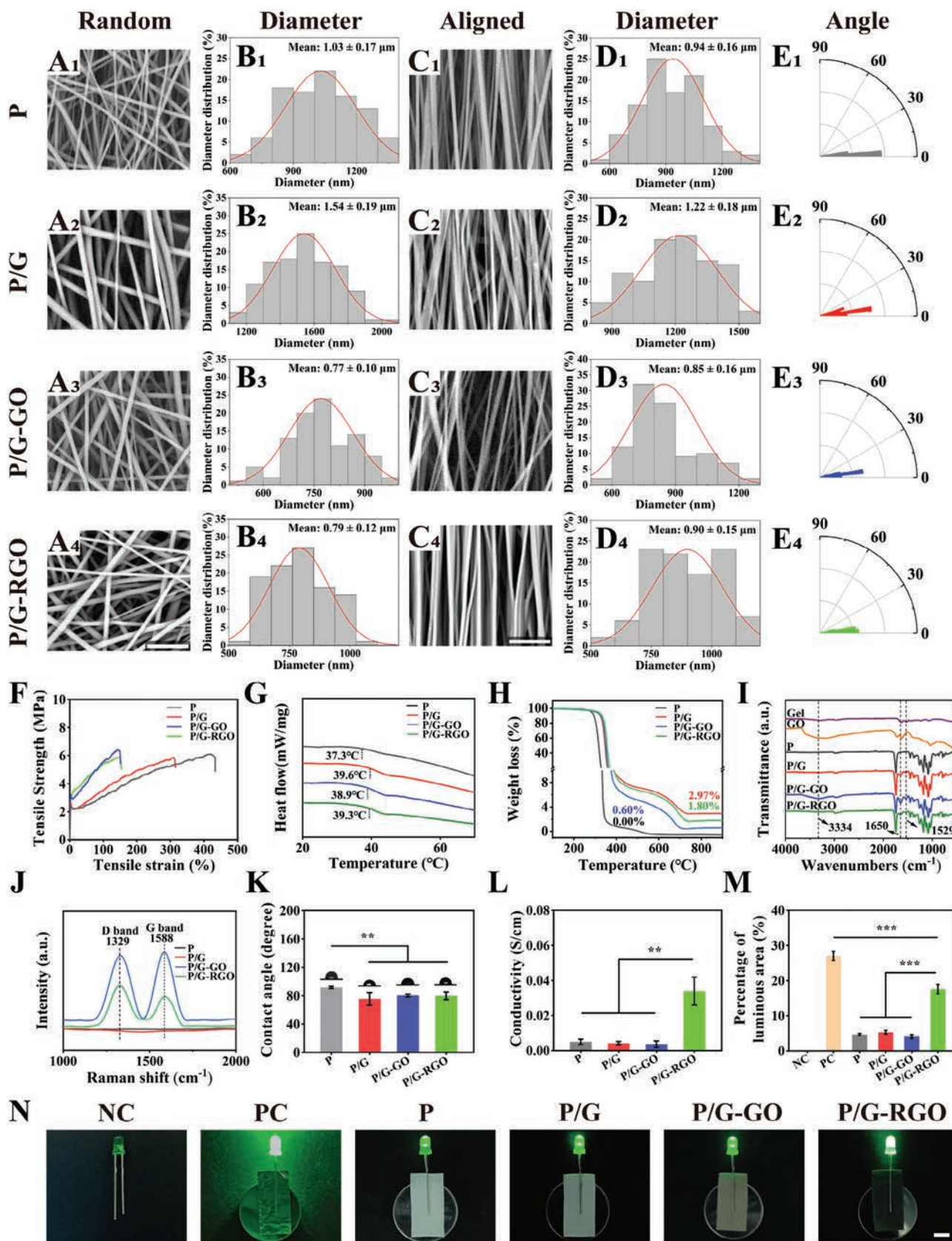
Electrospun membranes with an outer layer of random nanofibers and an inner layer of aligned nanofibers were smooth and bead-less (Figure 1A1–4 and C1C4). The diameters of the random layers were $1.03 \pm 0.17 \mu\text{m}$, $1.54 \pm 0.19 \mu\text{m}$, $0.77 \pm 0.10 \mu\text{m}$, and $0.79 \pm 0.12 \mu\text{m}$ for P, P/G, P/G-GO, P/G-RGO membranes (Figure 1B1–4). The diameters of the aligned layers were $0.94 \pm 0.16 \mu\text{m}$, $1.22 \pm 0.18 \mu\text{m}$, $0.85 \pm 0.16 \mu\text{m}$, and $0.90 \pm 0.15 \mu\text{m}$ for P, P/G, P/G-GO, P/G-RGO membranes (Figure 1D1–4). In addition, nanofibers of P/G-RGO still had a clear structure, indicating that the reduction of GO by L-ascorbic acid did not change the morphology. To assess the alignment of

the nanofibers, the distribution of the aligned nanofiber angle was evaluated. The angle of different aligned nanofibers was concentrated between 0° and 30° (Figure 1E1–4). There was no significant difference in the alignment of the nanofibers of the four groups of membranes, and it was also demonstrated that the addition of Gel, GO, or RGO did not affect the morphology and arrangement of the nanofibers.

The stress–strain curves showed that the breaking strain of the nanofiber membrane was significantly reduced from $452.71 \pm 27.19\%$ to $347.04 \pm 26.73\%$ after Gel addition. These results were consistent with the previous study.^[28] The breaking strain was further reduced after addition of GO (Figure 1F and Figure S1, Supporting Information). GO aggregated to make nanofibers more fragile, resulting in decreased strain, which was consistent with previous research.^[29] As shown in Figure 1G, the T_g of the P, P/G, P/G-GO, and P/G-RGO membranes was 37.3, 39.6, 38.9, and 39.3 °C, respectively. A temperature higher than T_g was required to guarantee the completion of the shape memory process, so 40 °C was chosen as the temperature of deformation. Furthermore, at a temperature lower than T_g , each NGC can maintain a persistent tube structure, so conduits can maintain the original tube structure within the body temperature range.

As shown in Figure 1H, the mass percentages of burning residues were 0%, 2.97%, 0.60%, and 1.80% for P, P/G, P/G-GO, and P/G-RGO membranes, respectively. The incorporation of Gel, GO, or RGO improved the thermal stability of the composite nanofibers. Moreover, the FTIR spectra (Figure 1I) showed that the characterized peaks around 3334 cm^{-1} , 1720 cm^{-1} , and 1610 cm^{-1} were -OH, C = O, and N-H telescopic vibration peaks of GO. The addition of Gel in P/G-GO made the peaks of C = O, N-H, and amide I (1631 cm^{-1}), amide II (1522 cm^{-1}) bonds in Gel superimposed on each other shifted at 1650 and 1529 cm^{-1} respectively, indicating that GO was successfully co-mingled into nanofibers. The spectrum of P/G-RGO nanofibers showed that the absorption peaks of -OH, C = O, and N-H were attenuated to different degrees, indicating that RGO was successfully reduced.^[30] To confirm the reduction of RGO, Raman spectra of four groups of membranes were also measured. As shown in Figure 1J, the spectra of P/G-GO nanofibers presented D band and G band of GO at 1329 and 1558 cm^{-1} . The D/G intensity ratios of P/G-RGO fibers were 1.39 which was greater than that of P/G-GO (0.95). The intensity of G band was higher than D band of P/G-GO membrane, while the intensity of the D band was higher than G band of P/G-GO membrane, indicating that the structure of graphene appeared and GO was effectively reduced to RGO.^[31]

In addition, membranes were also characterized by high resolution XPS spectra of C1s (Figure S2 and Table S1, Supporting Information). All samples exhibited three peaks at 284.8, 286.6, and 289.0 eV, which were ascribed to C = C/C-C, C-O, and -COOH groups, respectively.^[32] After calculating the area ratio of signal peaks in nanofibers, Figure S2 (Supporting Information) showed that the ratio of C-O and COOH groups in P/G nanofibers was larger than that of P nanofibers, indicating the incorporation of carboxyl groups into gelatin. After incorporation of GO, the area ratio of C-O group increased due to a large number of epoxide groups in GO. The area ratio of C-O and COOH groups in P/G-RGO was lower than that of P/G-GO membrane, indicating the presence of RGO. The TEM image showed that GO sheets were



distributed in nanofibers, further confirming the existence of GO and RGO (Figure S3, Supporting Information).

The WCA results (Figure 1K) suggested good wettability due to the addition of Gel, containing -NH and -COOH groups interacting with water molecules.^[33] Therefore, nanofibrous NGCs with Gel added, i.e., P/G, P/G-GO and P/G-RGO, were selected for the following experiments.

Aluminum foil was used as a positive control, and each group of materials was sandwiched between the LEDs and button cell batteries, and the higher the conductivity of the membranes, the stronger the LED emission. The LED alone emitted no light as negative control (NC), and the aluminum foil control group emitted the strongest light as positive control (PC) (Figure 1N). The percentage of LED-emitting area of the P/G-RGO membrane was significantly higher than that of the other membranes (Figure 1M). The conductivity calculated from the resistance values showed that the P/G-RGO membrane was significantly more conductive than the other membranes (Figure 1L). Meanwhile, in vitro degradation showed that all NGCs demonstrated a slow degradation rate and proper biodegradability. After the addition of Gel, the degradation rate of P/G, P/G-GO, and P/G-RGO NGCs became faster than that of P NGCs. Moreover, the multichannel structure of all NGCs remained stable after 60 days (Figure S4, Supporting Information).

2.2. The Shape Memory Property of NGCs

To verify the shape memory properties of the P, P/G, P/G-GO, P/G-RGO NGCs, the conduits were deformed into temporary planar shapes. Shape recovery of small tubes and large tubes was completed in 8 and 30 s, respectively, which were immersed in a water bath at 40 °C (Figure 2A). Three-channel nerve conduits with three internally nested tubes were finally obtained. The entire recovery process was rapid and repeatable. After five deformation cycles, all materials were still able to return to the tubular structure (please see Video S1, Supporting Information).

The R_r and R_f parameters of P, P/G, P/G-GO, and P/G-RGO nanofiber membranes after one cycle were presented in Figure 2B. R_r was above 89% of all membranes, and R_f decreased gradually from 93.94% of P to 71.85% of P/G, 56.32% of P/G-GO, and 59.40% of P/G-RGO with the addition of Gel and GO. In conclusion, the addition of G, GO, or RGO did not affect the shape recovery rate of membranes and still had good shape memory properties.

2.3. Evaluation of Neural Cell Outgrowth in NGCs

To investigate the effect of GO or RGO loading on nanofibers on cell proliferation with or without ES, SC, and PC12 cells were cultured on P/G, P/G-GO, and P/G-RGO NGCs. As shown in

Figure 3E, the number of SCs on P/G-RGO NGC was significantly higher than on the other two NGCs after 4 days. Additionally, cell proliferation on P/G-RGO NGCs was promoted by ES. After 7 days, the number of SCs on P/G-GO and P/G-RGO was higher than on P/G NGCs. Comparing the proliferation of PC12 cells on these nanofibers, PC12 cells showed better proliferative behavior on P/G-GO and P/G-RGO than on P/G NGCs (Figure 3F), which was consistent with SCs on different NGCs. In conclusion, P/G-RGO NGC was found to be the most effective for cell proliferation, especially with ES.

To observe cell–NGC interactions, fluorescence staining was performed after 7 days of culturing SCs and PC12 cells. The direction of these cells grown on aligned nanofiber membranes was aligned with the direction of the nanofibers, which is consistent with previous finding.^[34] To investigate the effect of ES on the differentiation of PC12 cells, the fluorescence images were counted for the percentage of differentiated cells and the length of differentiated axons (Figure 3A and Figure S5, Supporting Information). Cells elongated along the direction of nanofiber orientation after adhering and spreading on NGCs. The number of cells was higher on P/G-GO and P/G-RGO NGCs, especially on the P/G-RGO NGC with ES both SCs and PC12 cells. The SEM images of SCs and PC12 cells showed the similar results (Figure 3B). In addition, the morphology of PC12 and ES varied on different NGCs.

The SCs on RGO-containing conductive NGCs exhibited a tensile morphology growing along the oriented nanofibers, indicating that NGCs with suitable electrical conductivity could promote the maturation of SCs. Morphological changes in PC12 cells are closely related to their degree of differentiation. As shown in Figure 3A, the cells were fusiform-shaped and elongated neurites from the soma, confirming that the differentiation of PC12 cells was induced by ES. Moreover, the PC12 cells showed an oriented morphology of elongation along the aligned nanofibers. Compared with P/G-GO and P/G-RGO NGCs, PC12 cells on P/G-RGO NGCs with ES were more clearly differentiated with a higher percentage of differentiated cells and longer synapses, suggesting that RGO has a certain electrical conductivity and significantly promotes PC12 cell differentiation. In addition to P/G-RGO NGCs, PC12 cells on P/G and P/G-GO NGCs with ES also appeared to be partially differentiated, as the conductive nature of ions in the medium induced PC12 cell differentiation under electric field. In addition, the percentage of differentiated cells and the neurite length of PC12 cells on P/G-RGO NGCs were significantly greater than those on P/G and P/G-GO NGCs with ES (Figure 3G,H). The above studies demonstrated that conductive RGO-binding ES could effectively regulate the maturation and differentiation of SCs and PC12 cells.

To investigate the effect of different NGCs on the migration of SCs and PC12 cells, Transwell assay was used to study the migration of both cells. The number of SCs and PC12 cells seeded on P/G-RGO NGCs with ES was higher than other groups

Figure 1. Characterization of P, P/G, P/G-GO, and P/G-RGO nanofibers. A1–A4) SEM images of random nanofiber layer of tubes and B1–B4) diameter distribution of random nanofibers of tubes. C1–C4) SEM images of aligned fiber layer of tubes and D1–D4) diameter distribution of aligned nanofibers of tubes. E1–E4) Nightingale rose plots of the aligned nanofiber angle distribution for tubes and 0 ° represented the nanofiber parallel to the vertical axis. Scale bar: 10 μm. F) Tensile strength–strain curves, G) DSC curves, H) TGA curves, I) FTIR spectra, J) Raman spectra, K) WCA of P, P/G, P/G-GO, and P/G-RGO membranes. L) Conductivity and M) Percentage of luminous area of nanofibrous membranes. N) Conductivity observation of nanofiber membranes. Scale bar: 5 mm. * $p < 0.05$, ** $p < 0.01$, *** $p < 0.001$.

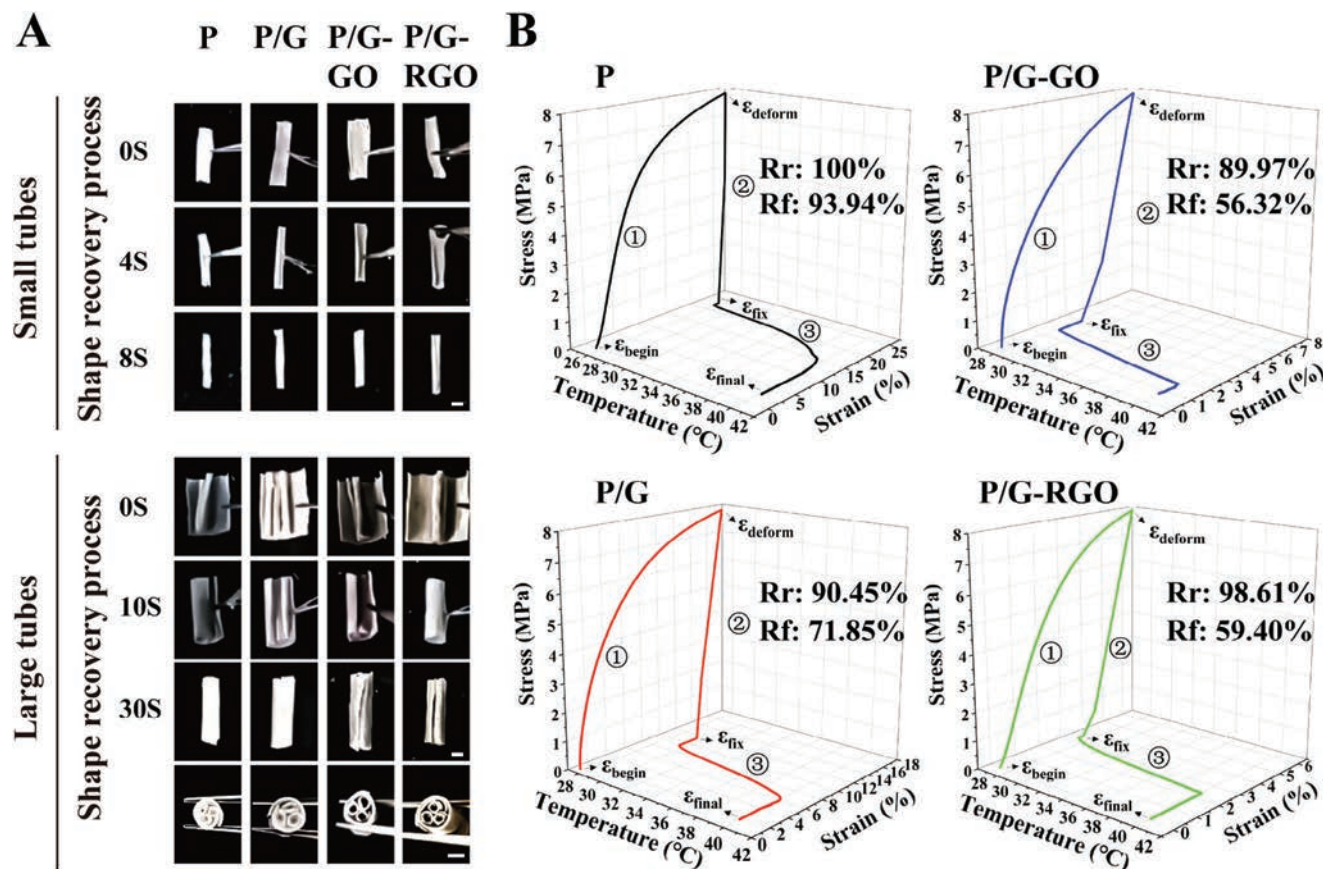


Figure 2. Evaluation of shape memory properties of different NGCs. A) Shape recovery process of small and large P, P/G, P/G-GO, and P/G-RGO tubes. Scale bars: 2 mm, 1 mm. B) Rr and Rf obtained from the DMA test of various samples.

(Figure 3C,D). Quantitative analysis of the migration results revealed that a significant difference in the proliferative ability of SCs was observed between P/G-GO, P/G-RGO, and P/G, normal control groups, and P/G-RGO combined with ES groups showed the most pronounced effects (Figure 3I). The analysis of PC12 cell migration results also led to consistent conclusions (Figure 3J).

The distribution of SCs seeded on different conduits was assessed by fluorescence staining after incubation for 5 days (Figure 3K). Fluorescence staining of cross-sections of conduits was performed to observe the structure of conduits and the distribution of cells. In each group, SCs were able to grow and remain viable in each channel of these structurally stable conduits. Thus, this conduit molding approach provided a favorable microenvironment for cell distribution and axonal extension during nerve regeneration.

2.4. Myelin Gene Expression of SCs Cultured in NGCs

It is critical for peripheral nerve regeneration that SCs wrap around regenerated axons to form myelin sheaths. The genes can be categorized into two groups based on the degree of expression in mature SCs. *NCAM* is expressed only in immature SCs and decreases with SCs myelination. In contrast, *Krox20*, *PMP22*, and *NGF* are increased with myelination (Figure 4A).

As shown in Figure 4B, gene expression of *Krox20*, *PMP22*, and *NGF* was higher on P/G-RGO NGCs than on TCP, P/G, and P/G-GO NGCs. In reverse to the above genes, gene expression of *NCAM* was lower on P/G-RGO NGCs than on TCP, P/G, and P/G-GO NGCs. Moreover, gene expression of *Krox20*, *PMP22*, and *NGF* increased on P/G-RGO NGCs, and *NCAM* decreased on P/G-RGO NGCs significantly after ES. These results showed that conductive P/G-RGO NGCs were more favorable for SCs myelination under the condition of ES.

2.5. Histological Analysis of Regenerated Sciatic Nerves

The electrospun NGCs were subcutaneously implanted in SD rat to evaluate the biocompatibility in vivo (Figure S6, Supporting Information). H&E staining revealed a moderate inflammatory response of three grafts at 2 weeks and there was no significant difference in inflammatory response among them. Inflammatory cells around the grafts were significantly reduced in all groups at 4 weeks, indicating that the inflammatory response was alleviated. After 4 weeks, fewer inflammatory cells clustered around the P/G-GO and P/G-RGO membranes than around the P/G membrane (Figure 5J). Masson's trichrome staining indicated increased deposition of collagen covering the NGCs from

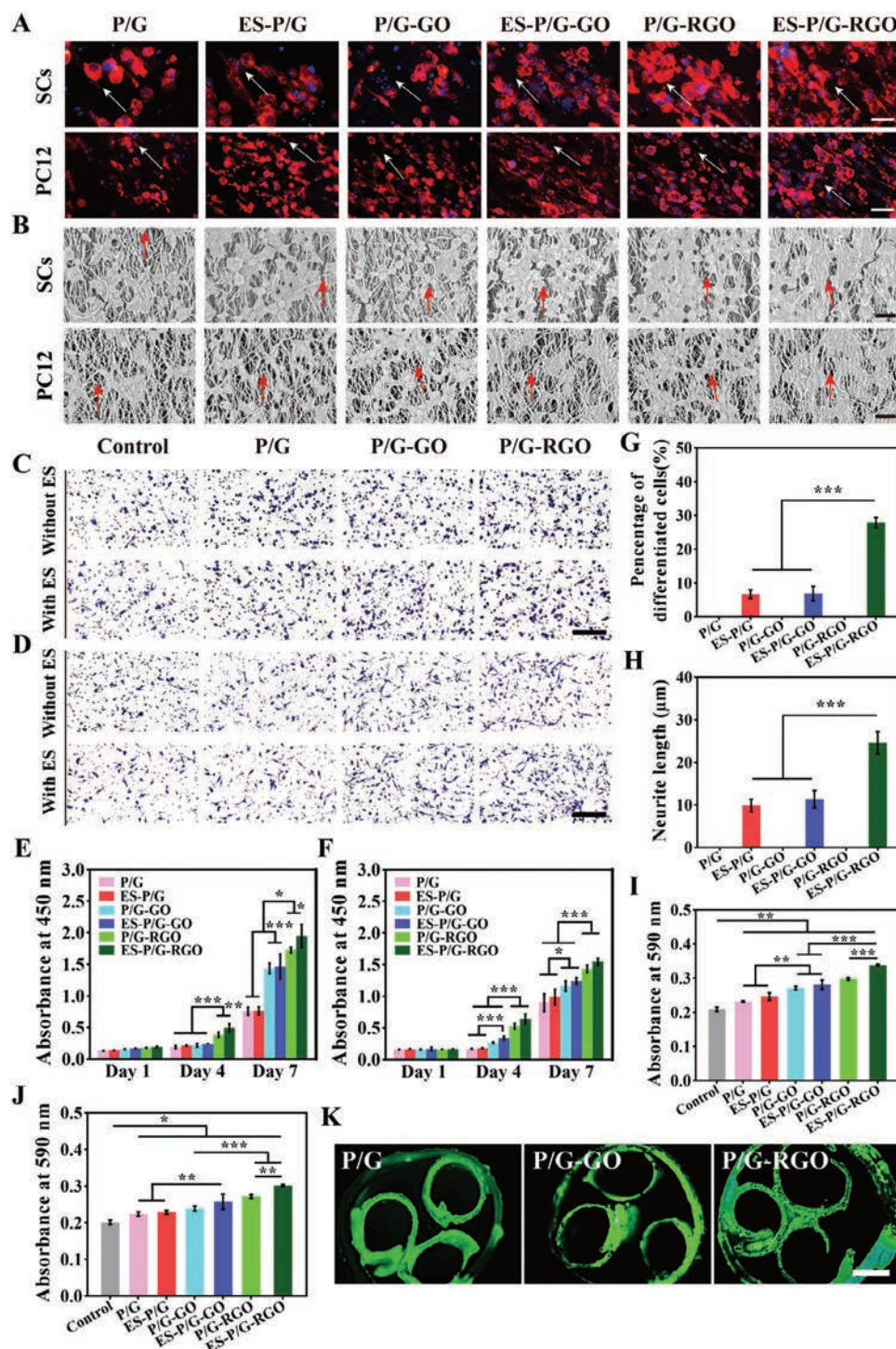


Figure 3. SC and PC12 cells proliferation and migration on various conduits. A) Immunofluorescence images of SCs and PC12 cells in P, P/G, P/G-GO, and P/G-RGO conduits after incubation for 7 days. The cytoskeleton was stained with TRITC-phalloidin (red), and the nuclei were stained with DAPI (blue). Scale bar: 50 μm . B) SEM images of SCs and PC12 cells co-cultured in various NGCs after 7 days. Scale bar: 20 μm . Images of C) migrated SCs and D) PC12 cells on different substrates with or without ES. Cells were stained purple with crystal violet. Scale bar: 200 μm . Proliferation of E) SCs and F) PC12 cells in different conduits. Statistics of G) differentiated cells and H) neurite length of PC12 cells based on immunofluorescence images. Calculation of migration rate of I) SCs and J) PC12 cells, respectively. K) Distribution of SCs in different conduits with the persistent shapes after incubation for 5 days. Scale bar: 500 μm . * $p < 0.05$, ** $p < 0.01$, *** $p < 0.001$.

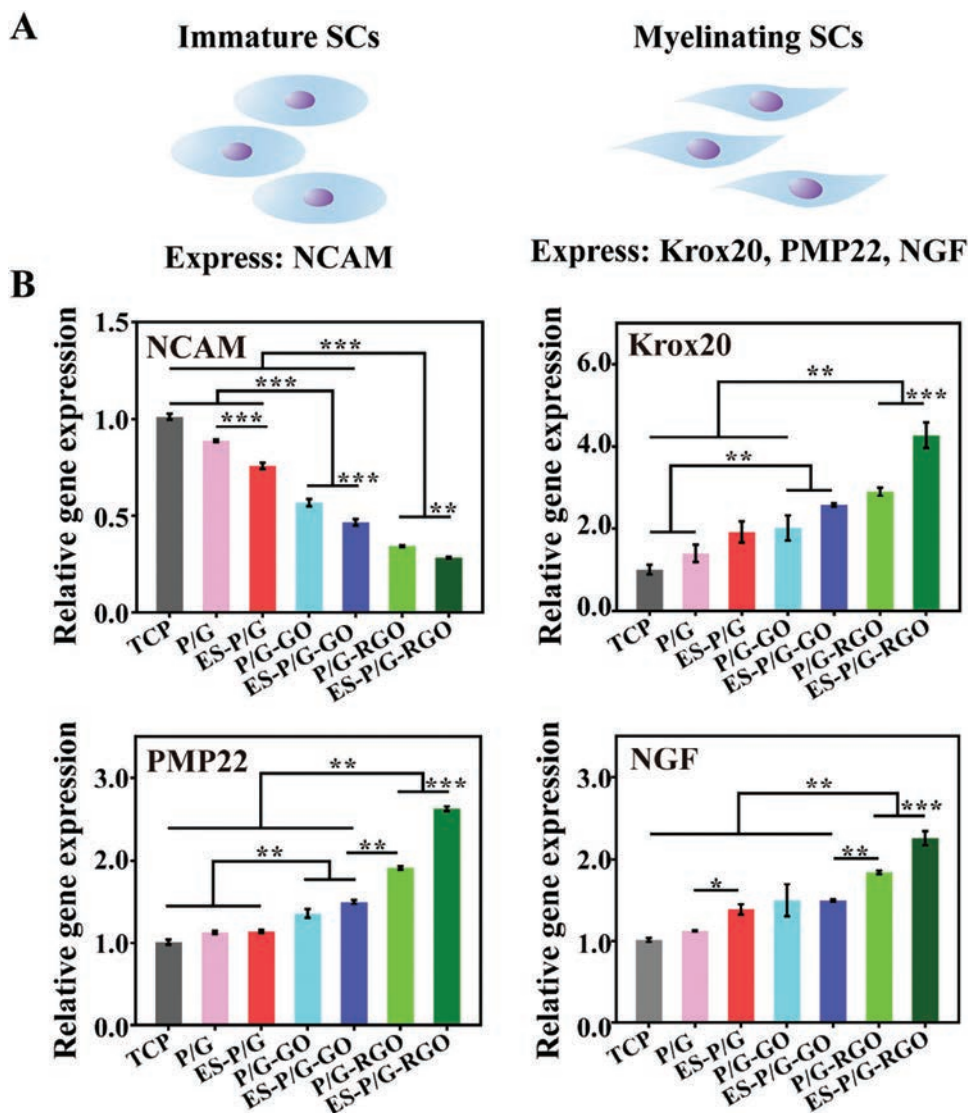


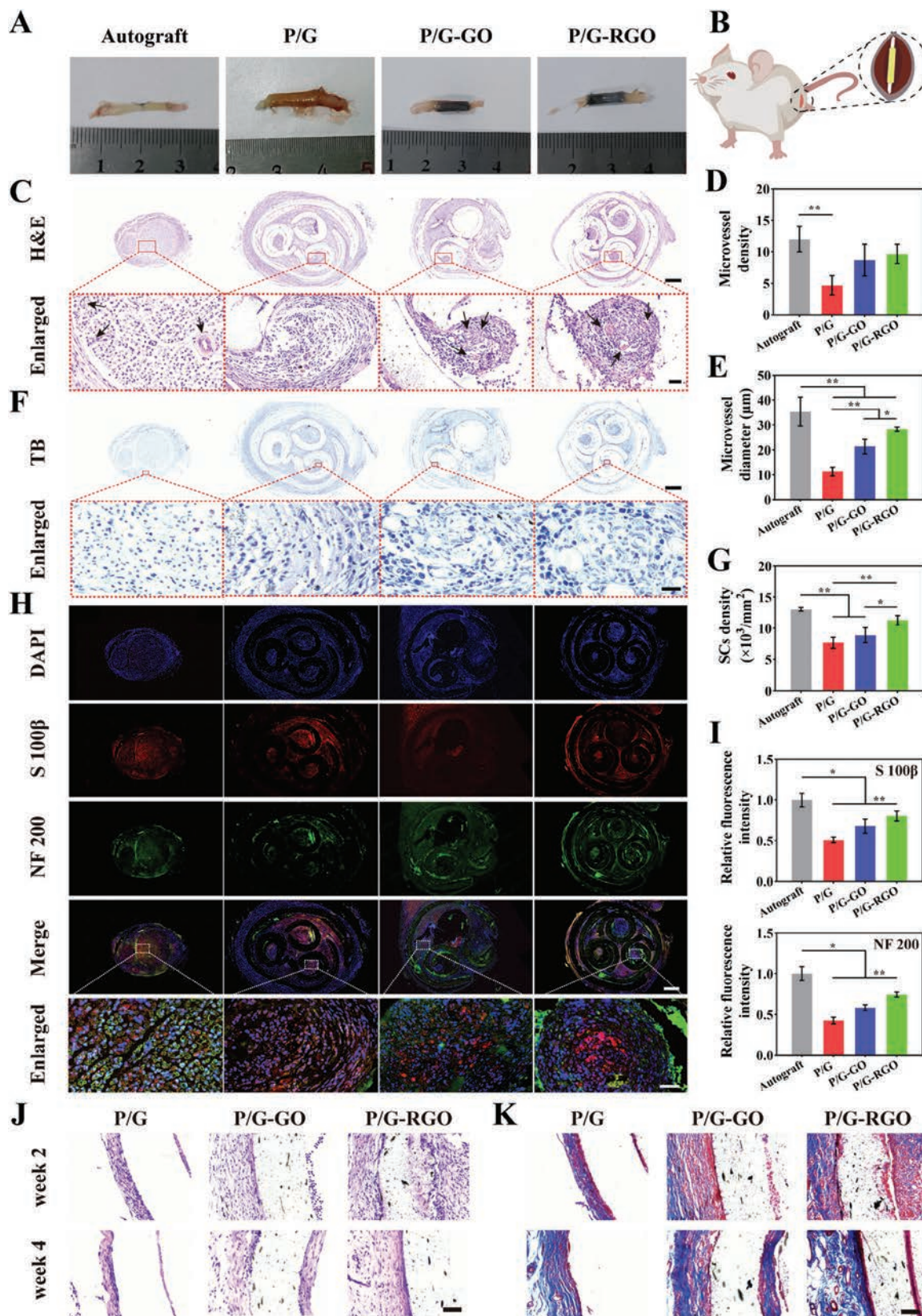
Figure 4. Myelin gene expressions of SCs cultured on various conduits with or without ES. A) Gene expression changes in SCs at different stages. B) The qRT-PCR analysis of NCAM, Krox20, PMP22, and NGF gene expressions of the SCs on different NGCs after 5 days. The gene expressions of SCs on TCP as control. * $p < 0.05$, ** $p < 0.01$, *** $p < 0.001$.

week 2 to 4, and newly formed capillaries surrounding all NGCs (Figure 5K).

To estimate the regenerated nerve tissue in different groups, conduits were implanted into 10 mm nerve defects in rat sciatic nerves for 12 weeks (Figure 5A,B). Cross-sections of the regenerated nerves were taken at the mid-position to evaluate axonal regeneration. As shown in Figure 5C, the H&E staining images indicated that the regenerated tissue extended into all NGCs. In addition, newborn blood vessels with red blood cells inside were found between the regenerated nerve tissue in all groups (Figure 5C). The density and diameter of the newborn microvessels were calculated as shown in Figure 5D,E, respectively, indicating the microvessel-promoting effects of GO and RGO.

TB staining showed that large amounts of SCs were observed in all groups (Figure 5F). Furthermore, the density of the P/G-

RGO group was similar to that of the autograft group and significantly better than that of the P/G and P/G-GO NGCs (Figure 5G). The expression level of the SC-specific marker S-100 β and the neurofilament marker NF-200 of the regenerated nerves were examined by immunofluorescence staining at 12 weeks after surgery (Figure 5H). The S-100 β and NF-200 proteins were expressed in all groups, confirming the formation of myelin sheaths composed of SCs and growth of new axons. As shown in Figure 5I, the relative fluorescence intensities of S-100 β and NF-200 were the highest in the autograft group. In the conduit graft groups, the expression level of these markers was much higher in the P/G-RGO conduit than in the P/G conduit. Apparently, the inclusion of RGO supported a higher density of SCs and remyelination compared to the other conduits, which further supported axon regeneration.



2.6. Functional Evaluation of the Regenerated Sciatic Nerve

Footprint assessment was used to evaluate the degree of recovery of the regenerated nerve (Figure 6A). The footprints of P/G-GO and P/G-RGO NGCs showed noticeable recovery and were closed to autografts (Figure 6B). SFI values displayed negligible differences between P/G-GO, P/G-RGO conduits and autografts, but autografts were significantly higher than those of P/G NGCs (Figure 6E). Atrophy of the gastrocnemius muscle, one of the target tissues of the sciatic nerves, was used to assess the functional recovery of the regenerated nerves. As confirmed in Figure 6C,F, gastrocnemius muscle atrophy occurred in all conduits compared to the autograft groups. The TSM weight of the P/G-RGO NGCs was much heavier than that of the transplanted conduits. In addition, Masson's trichrome staining confirmed widespread collagen deposition around the muscles in the P/G groups (Figure 6D). Statistically, the percentage of collagen area in the P/G-GO and P/G-RGO conduits was significantly less than that in the P/G groups (Figure 6G). The average area of muscle fibers of the P/G-RGO NGCs was not significantly different from that of the autograft group, and was significantly better than that of the P/G and P/G-GO NGCs (Figure S7, Supporting Information). Taken together, these results demonstrated that the critical roles of GO and RGO in promoting the functional recovery of peripheral nerves, and the conduits containing RGO have greater transcendence in guiding nerve regeneration.

3. Discussion

Peripheral nerve injury (PNI) remains a critical clinical problem, affecting millions of people worldwide annually.^[35] Many scientists have turned to biomaterials to repair PNI because of the drawbacks of autografts.^[36] In neural tissue engineering, the conduit acts as a bridge between the nerve ends and protects the regenerating nerve. However, the use of single-tubular conduits results in poor longitudinal guidance of nerve regeneration. Multichannel NGCs have been explored to mimic the fascicular architecture of the nerve and promote axon extension.^[37] During nerve regeneration, the grafted multichannel NGC may collapse and deform as the material degrades. Thermo-responsive SMPs could maintain a persistent tube structure over a range of temperature changes in the body. Previous studies have shown that axons require a stable substrate to grow, making thermo-responsive shape memory NGC with persistent shape was an excellent candidate for long-gap nerve regeneration.^[14] Meanwhile, autologously transplanted human sciatic nerves showed a maximum stress of 1930 ± 50 kPa and a strain of $18.00 \pm 1.30\%$ as reported.^[38] The P, P/G, P/G-GO, and P/G-RGO NGCs meet the necessary mechanical thresholds for neural conduits. These NGCs not only provide mechanical support for nerve regeneration, but also facilitate the realization of the shape memory func-

tion of SMPs. Given these requirements, a three-channel shape-memory nerve conduit was designed. The results of the in vitro degradation and in vivo transplantation assay showed that the NGC could maintain structural stability without collapsing or deforming during nerve regeneration.

Many studies have shown that conductive materials can effectively promote the repair of peripheral nerves after injury, mainly due to their important role in transmitting signals between nerve systems, stimulating the proliferation and differentiation of nerve cells, and promoting the reconstruction of the physiological environment of peripheral nerve regeneration.^[39,40] The difficult dispersion of the conductive material graphene affects its application in nerve tissue engineering. GO improved dispersion in polar solvents due to possible hydrogen bonding compared to graphene, which supports a high processability.^[26] Furthermore, oxygen functionalities in GO break the sp^2 conjugation and the π - π bond and facilitate the form of hydrogen bonding, resulting in stronger cell attachment.^[41] Recently, Zhao et al. reported an electrodeposition of chitosan/GO conduit to improve biocompatibility and bioactivity for glial cells.^[42] Bioelectrical signals are integrated into nerve conduits to mimic native nerve tissue. GO is less conductive compared to graphene and RGO, which is reduced to restore the electrical conductivity. It has been shown that the electrical conductivity of NGCs is greatly enhanced when GO is reduced to RGO, and the ability to promote cell proliferation and support neural synapse growth is also improved. A silk fibroin/poly (L-lactic acid-co-caprolactone) NGC was coated with GO and reduced to RGO to achieve higher electrical conductivity, which elevated myelination of SCs and induced differentiation of PC12 cells in combination with ES.^[43]

Furthermore, neurons can conduct nerve impulses through endogenous ES. Conductive NGCs play a role in nerve repair by contacting electrically active nerve tissue and then transmitting bioelectricity in peripheral nerves to accelerate nerve repair. The RGO incorporated into the NGCs provided a medium for ES delivery and was expected to enhance the bioactivity of the NGCs. The possible reason why RGO combined with ES was beneficial to the biological function of SCs was that π - π bonds after reduction of RGO improved metabolic activity and benefited cell growth in terms of CCK-8 assay and gene expressions.^[44] Immunofluorescence staining showed that RGO combined with ES effectively promoted the differentiation of PC12 cells, which was in line with previous research.^[45] Many studies have been conducted on the mechanism of action of ES in neuronal cells, and the widely accepted view is that the electrical coupling reaction between the cell and the material contact surface upregulates Ca^{2+} related channels. The proliferation and differentiation of neuronal cells are affected by the concentration of intracellular Ca^{2+} .^[46] ES can regulate the open or closed state of the Ca^{2+} channel to alter the intracellular concentration of Ca^{2+} , thereby altering the transmembrane potential of neuronal cells.

Figure 5. Implantation of nerve conduits and morphological assessment of the regenerated nerves. A) Photographs of harvested nerve conduit grafts at 12 weeks after surgery. B) Schematic illustration of conduit implantation in the SD rat sciatic nerve defect model. C) H&E staining of cross-sections of regenerated nerve tissue after 12 weeks (closed circles with deep staining indicated by black arrows). Scale bars: 400 μ m, 50 μ m. The quantitative analysis of D) density and E) diameter of newborn microvessels. F) TB staining of cross sections of regenerated nerve tissue at 12 weeks. Scale bars: 400 μ m, 20 μ m. G) Quantitative analysis of the density of SCs. H) Immunofluorescence staining of S-100 β (red), NF-200 (green), and nuclei (blue) at 12 weeks post-transplantation. Scale bars: 400 μ m, 40 μ m. I) Relative fluorescence intensity of S-100 β and NF-200. J) H&E and K) Masson's trichrome staining of subcutaneous implantation cross sections after 2 and 4 weeks. Scale bar: 50 μ m. * p < 0.05, ** p < 0.01, *** p < 0.001.

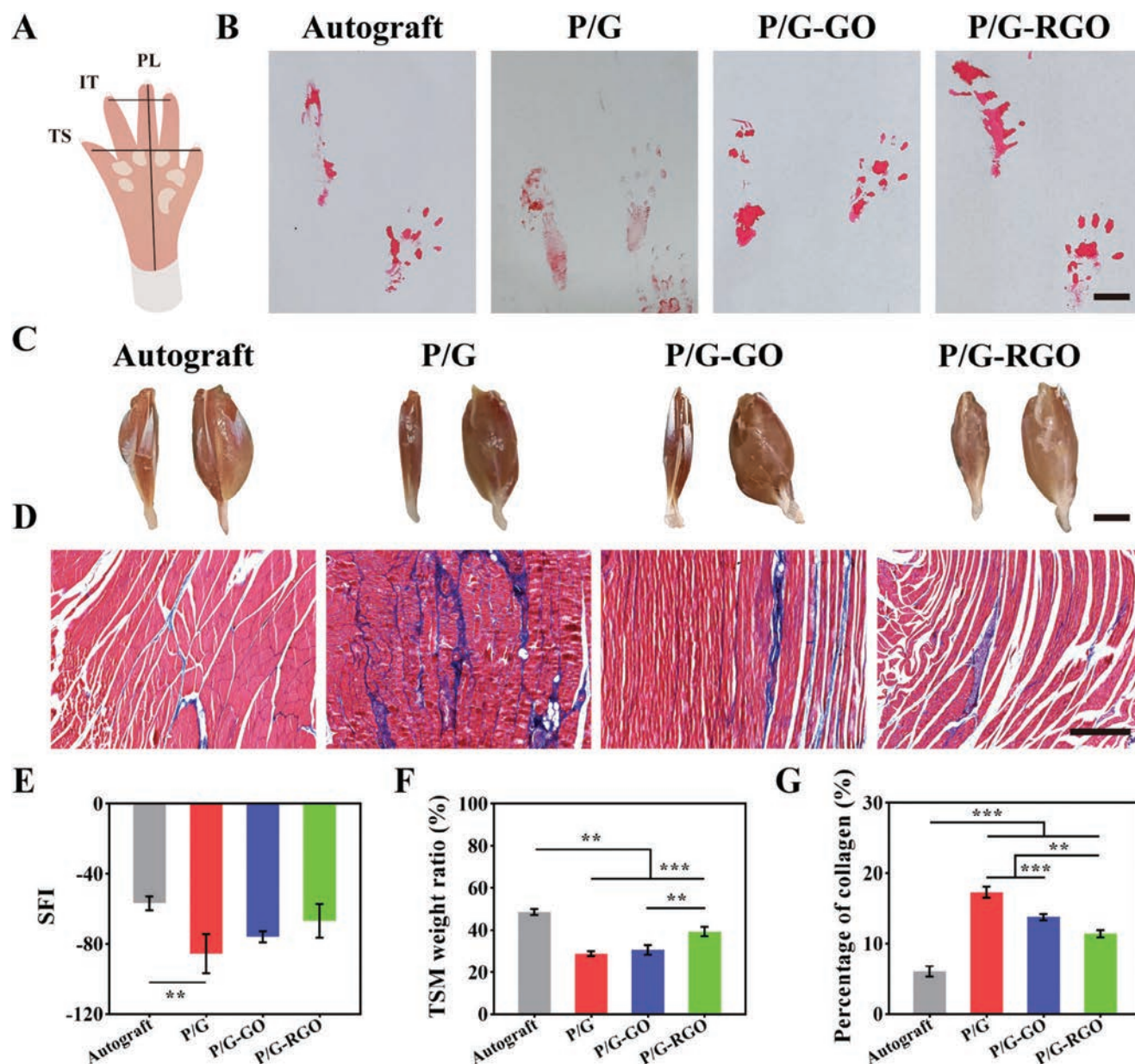


Figure 6. Functional evaluation of the regenerated nerves at 12 weeks post-implantation. A) Schematic illustration of walking track assessment. B) Representative images of footprints. Scale bar: 10 mm. C) Representative images of harvested gastrocnemius muscles from both hind limbs at 12 weeks post-surgery. Scale bar: 10 mm. D) Images of cross-sections of gastrocnemius muscles stained with Masson's trichrome. Scale bar: 200 μ m. Quantitative analysis of E) SFI, F) TSM weight ratio, G) and percentage of collagen. * $p < 0.05$, ** $p < 0.01$, *** $p < 0.001$.

The influx of Ca^{2+} into cells through Ca^{2+} channels can activate various signaling pathways related to neuronal proliferation and differentiation.^[47] The definitive mechanism of the effect of conductive NGCs combined with ES on the behavior of SCs requires further studies.

Peripheral nerve regeneration is a process that involves the coordination of Schwann cells, axons, macrophages, and blood vessels.^[48] Difficulties in regeneration caused by inflammatory responses at the injury site and insufficient vascularization may also occur during nerve repair. The results of the H&E and Masson's trichrome staining of the NGCs showed a trend to-

ward decreased inflammatory cells around all grafts from 2 to 4 weeks, and newly formed capillaries surrounding all grafts at 4 weeks, indicating good biocompatibility in vivo and the ability to promote angiogenesis.^[49] Angiogenesis after nerve injury is crucial for the guidance of SCs and recovery of general nerve function.^[50,51] The density and diameter of the regenerated blood vessels of the P/G-RGO NGC were close to the autograft, which may indicate that the presence of RGO promotes blood vessels regeneration.^[52]

Overall, the thermo-responsive shape memory function of these conduits helped repair nerve defects over long-gap and

larger-diameter. In this study, we effectively demonstrated that the conductive conduit containing RGO promoted the proliferation and differentiation of nerve cells, the regeneration of myelin sheaths and axons, and the recovery of nerve function. We propose that the P/G-RGO conduit will be a viable alternative to autograft therapy.

4. Conclusion

In summary, a shape-persistent conductive NGC was fabricated by electrospinning using a thermo-responsive shape memory polymer PLMC and RGO. The multichannel structure with aligned nanofibers provided topographical cues for axon elongation, and maintained the stable tube shape without deformation in the physiological temperature range. Conductive NGC combined with ES promoted growth, proliferation, migration and myelination of SCs, and differentiation of PC12 cells. These evaluations, involving H&E, TB, immunofluorescence staining of nerve regeneration, and recovery of nerve function analysis consistently indicated that conductive P/G-RGO conduits promoted peripheral nerve repair close to that of the autograft. The P/G-RGO NGCs with the characteristics of stable structure and simple preparation, are expected to repair long-gap and large-diameter nerve defects.

5. Experimental Section

Materials: Poly (lactide-co-trimethylene carbonate, PLMC, LA: TMC = 7:3) was purchased from Jinan Daigang Co., Ltd. (Jinan, China). Gelatin (Gel, type II, 48722-500G-F) was obtained from Sigma-Aldrich (US). Graphene oxide (GO, 1034343-98-0) was purchased from Macklin Co., Ltd. (Shanghai, China). L-Ascorbic acid (50-81-7) was purchased from China National Pharmaceutical Group (Shanghai, China). 1,1,1,3,3,3-Hexafluoro-2-propanol (HFIP, 920-66-1) was purchased from Shanghai Darui Fine Chemical Co., Ltd. (Shanghai, China). Schwann 96 cells (SCs) and PC12 cells were provided by the Institute of Biochemistry and Cell Biology (Shanghai, China).

Fabrication and Characterization of NGCs: Nanofiber Membranes: The PLMC was dissolved in HFIP to obtain 12 wt% spinning solution and named as P. To prepare PLMC/Gel (P/G) solution, PLMC and Gel (9:1 w/w) were dissolved in HFIP to obtain 12 wt% (w/v) solution. The 1 wt% (accounting for the mass ratio of the polymer) sonicated GO nanoparticles were mixed in 12 wt% PLMC and Gel (9:1 w/w) and dissolved in HFIP (P/G-GO). All membranes were fabricated by electrospinning (Yongkang Leye Technology Development Co., Ltd. SS-3556H, Beijing, China). The electrospinning parameters were as follows: flow rate was 1 mL h⁻¹, needle size was 20 G, voltage was 14 kV, collector speed was 3000 rotations per minute (rpm) to collect aligned nanofibers and 200 rpm to collect random nanofibers. Then, the P/G-GO nanofiber membrane was reductive to P/G-RGO by L-ascorbic acid for 48 h at room temperature. The P, P/G, P/G-GO, P/G-RGO membranes were vacuum-dried overnight to remove residual solvents.

Fabrication of Multichannel NGCs: The P, P/G, P/G-GO, P/G-RGO membranes were cut to predefined sizes of 10 mm × 20 mm and wrapped on steel rods. The aligned layer was in contact with the steel rod and the nanofiber orientation was along the longitudinal axis of the steel rod. Subsequently, the steel rod was treated in an oven at 60 °C for 30 min to reshape the tubular structure. These tubes with different inner diameters (0.8 and 2 mm) were obtained by changing the diameters of the steel rods. The tubes were then deformed into temporary planar structures at 0 °C under external stress. The small tubes (0.8 mm) were immersed in distilled water to recover their initial shape at 40 °C. Three small and parallel

tubes were positioned on a large membrane at 0 °C, and changed shape at 40 °C. Within this phase, the large membrane deformed, regained its original tube structure and enveloped the three small tubes to form the NGC (Figure 7).

Characterization of NGCs: The shape recovery of the P, P/G, P/G-GO, and P/G-RGO NGCs, including the recovery process from the temporary planar shape to persistent tubular shape, were recorded by a digital camera. Dynamic mechanical analysis (DMA) (TA instruments Q800, USA) was performed to quantify the shape memory properties of different nanofiber membranes. Specifically, the 10 mm × 20 mm membranes were heated at 60 °C for 30 min to form an initial flat shape. The program of DMA was set to 25 °C, and the nanofiber membranes were slowly stressed to 8 MPa at a rate of 1 MPa min⁻¹ to change shape below the T_g. Then the applied stress was removed, and the shape fixity ratio (R_f) of nanofiber membranes was measured. The ambient temperature was increased from 25 to 40 °C at a rate of 5 °C min⁻¹, so the membranes were returned to fixed initial flat shape in order to evaluate the shape recovery ratio (R_r) of the membrane.

The morphologies of the P, P/G, P/G-GO, P/G-RGO nanofibers were identified by scanning electron microscopy (SEM, Hitachi TM-1000, Japan) after sputter coating with gold. At least 100 nanofibers randomly selected from each sample were measured for average diameter and angle distribution of aligned nanofibers by Image J software (National Institutes of Health, v1.8.0, USA). The angle distribution of aligned nanofibers pertains to the absolute value to the horizontal axis.^[53] The mechanical properties of the P, P/G, P/G-GO, P/G-RGO membranes (10 mm × 30 mm, n = 6) were measured using a material testing machine (HY-940FS, China).

Thermal properties of P, P/G, P/G-GO, P/G-RGO membranes were determined by differential scanning calorimetry (DSC) on a TA instrument (204 F1 Netzsch, Germany) according to a previous report.^[15] Thermogravimetric analysis (TGA) of the P, P/G, P/G-GO, P/G-RGO membranes was carried out to obtain TGA and DTG curves using a Thermogravimetric Analyzer (TGA8000, Shanghai, China).

To confirm the loading and reduction of GO, these membranes were characterized respectively by Fourier transform infrared (FTIR, Nicolet Instrument, Madison, USA) and Raman spectrometer (Via-Reflex Renishaw plc, England). The loading of GO in P/G-GO was further identified by transmission electron microscopy (TEM, JEOL, JEM-2100, Japan). X-ray photoelectron spectroscopy (XPS, Kratos Analytical, UK) was used to determine elements and functional groups on the surface of nanofiber membranes.

The water contact angle (WCA) of the P, P/G, P/G-GO, P/G-RGO nanofibers was evaluated using a contact angle goniometer (OCA40, Dataphysics, Germany) to determine the surface hydrophilicity. To determine the degradation properties and structural stability of NGCs in vitro, each conduit was immersed in a centrifuge tube containing 2 mL PBS, then the tubes were shaken at 100 rpm at 37 °C for 60 days. These conduits were rinsed with deionized water and freeze dried to measure degradation behavior.

A light emitting diode (LED) and a button cell battery were used to determine the electrical conductivity of the P, P/G, P/G-GO, P/G-RGO membranes in the wet state. And the electrical resistance of the membranes was determined by the four-probe method (ST25588-F01, China) in wet state (n = 6).

Biocompatibility and Biological Function In Vitro: Hemocompatibility: The hemocompatibility of P, P/G, P/G-GO, P/G-RGO membranes was investigated with 2% (v/v) erythrocyte suspension which obtained from Sprague-Dawley (SD) rat. Briefly, 2 mL fresh anticoagulated whole blood was diluted with 5 mL normal saline and centrifuged at 3000 rpm for 10 min. The erythrocytes were washed five times with normal saline. Then 10 mg membranes were preheated at 37 °C for 30 min in 10 mL normal saline. Before gently mixing, 2% (v/v) erythrocytes were dripped into the prepared samples. These solutions were centrifuged to deposit intact erythrocytes and incubated at 37 °C for 1 h. Photographs of 500 μL supernatant in tubes were taken, and the absorbance of the supernatant was measured at 540 nm (n = 6). Distilled water and normal saline were used as positive and negative controls, respectively. The hemolysis ratio was calculated using the following Equation (1):

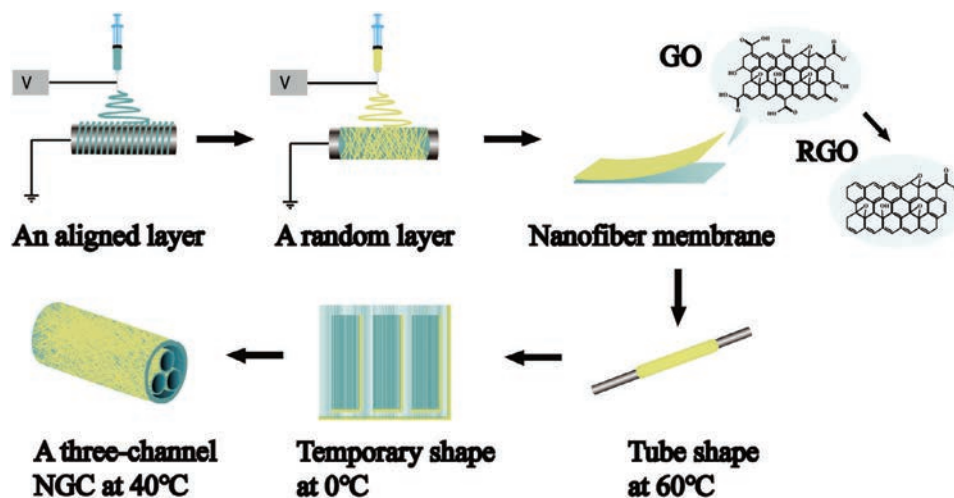


Figure 7. Schematic illustration of the fabrication of the three-channel NGC.

$$\text{Hemolysis ratio (\%)} = \left(\frac{A_s - A_n}{A_p - A_n} \right) \times 100 \% \quad (1)$$

where A_s represents the OD values of samples, while A_p and A_n indicate the corresponding OD of positive and negative control groups.

Cytocompatibility of NGCs: At first, P/G, P/G-GO, P/G-RGO membranes were preheated to form tubes at 60 °C for 30 min and unfolded to temporary flat structures at 0 °C. SCs suspension was prepared and seeded on the P/G, P/G-GO, P/G-RGO membranes at room temperature. The number of cells in each small and large membrane was 3×10^3 and 1×10^4 cells per well, respectively. The preparation process of NGCs of loaded cells was completed in two steps. First, three small membranes were placed in a 40 °C cell culture incubator for 2 min to prepare small tubes. Then, three small tubes were removed and placed on a large membrane at room temperature. Finally, the above samples were placed in an incubator at 40 °C for 5 min, and the three small tubes were wrapped by a large automatically curled membrane to prepare multichannel NGCs. After completion of shape memory, the cell-laden NGCs were transferred to a 37 °C cell culture incubator for 5 days. Finally, the NGCs were stained with Calcein-AM, followed by observation under a fluorescence microscope (LEICA, DMi8, Germany).

The Effects of Different NGCs on Cell Behavior via ES: To evaluate the effects of P, P/G, P/G-GO, P/G-RGO NGCs on cell behavior via ES, SC and PC12 cells were cultured on NGCs and incubated for 24 h to allow attachment prior to ES. ES was applied between two parallel electrodes that were led by aluminum foil as lead wires. A steady electric field of 100 mV cm^{-1} was applied based on physiological electric fields and previous reports using a direct current power supply (HSPY-36-03, China) for 1 h per day.^[54]

To evaluate the survival of SC and PC12 cells in the P, P/G, P/G-GO, P/G-RGO NGCs, the viability of the cells was determined by cell counting kit-8 (CCK-8, C0038, Beyotime, China) following the manufacturer's instructions after incubation at 1, 4, and 7 days. At each time point, the optical density (OD) of the samples was measured by the ELISA plate reader (Epoch TM, BioTek, USA) at 450 nm ($n = 3$). To appraise cell morphology and density, NGCs were fixed by 4% paraformaldehyde (PFA) solution (Sigma-Aldrich, USA) and stained with tetraethyl rhodamine isothiocyanate labelled Phalloidin (TRITC, 40734ES75, Yeasen, China) and 4,6-diamidino-2-phenylindole (DAPI, C0065, Solarbio, China), and observed by fluorescence microscope. The NGCs were dehydrated with graded ethanol for morphological observation and analysis by SEM.

The P, P/G, P/G-GO, P/G-RGO NGCs were placed at the bottom of 24-well Transwell cell culture plates and fetal bovine serum (FBS)-free cell culture medium was added to each well, followed by the placement of the Transwell chambers. The suspension of SC and PC12 cells of 1×10^4 cells

per well were droplets to the upper surface of the chambers. After incubation for 24 h, cells were fixed with 4% PFA for 30 min, and the appropriate amount of crystal violet staining solution was added for 10 min. The excess staining solution and non-migrated cells on the upper surface of the chambers were wiped off with a cotton swab, and the migration of the cells was observed under a light microscope. The chambers were placed in new 24-well plates and 10% (v/v) acetic acid solution dissolved the crystalline violet dye in the cells that had migrated to the lower surface of the chambers. The OD values corresponding to each well were measured at 590 nm after aspiration of the dissolved solution. The migration rates of SCs and PC12 cells were calculated from OD values.

To study the effects of ES on PC12 cell differentiation, PC12 cells were seeded separately on each group of NGCs separately at 8×10^3 cells per well. ES was performed at 7 days with 100 mV cm^{-1} electric field for 1 h per day and NGCs without electrical stimulation were used as control groups. Cells were fixed by 4% PFA solution and stained with TRITC-Phalloidin and DAPI and observed by fluorescence microscope. The number and neurite length of differentiated PC12 cells were measured using Image J software.

qRT-PCR: To evaluate the myelination of SCs cultured on the P, P/G, P/G-GO, P/G-RGO NGCs with or without ES, gene expression of *NCAM*, *NGF*, *PMP22*, and *Krox20* was examined by quantitative real-time PCR after 5 days of culture. Primer sequences are listed in Table S2 (Supporting Information), and gene expression was analyzed by the $2^{-\Delta\Delta C_t}$ method.

Animal Implantation: Sprague Dawley rats (SD) rats (200–250 g) were used to study peripheral nerve repair of autografts, P/G, P/G-GO, and P/G-RGO NGCs. All surgical procedures were performed in accordance with the Institutional Animal Care and Use Committee (IACUC:2022AW032) of the Shanghai Jiao Tong University. Sciatic nerve defects of 10 mm were created from each rat to generate an artificial nerve defect and then bridged with corresponding nerve conduits. For the autograft group, the excised nerve was flipped 180° and re-bridged. The rats were randomly divided into 4 groups: P/G, P/G-GO, P/G-RGO NGCs and autograft. All the rats were sacrificed at 12 weeks after surgery by intraperitoneal injection of pentobarbital sodium overdose. Rats were sacrificed by intraperitoneal injection of pentobarbital sodium 12 weeks after operation.

To confirm in vivo biocompatibility and shape-persistent of different nerve conduits, subcutaneous implantation models of SD were established as a preliminary experiment. The specific experimental protocol was to implant these NGCs into the left and right subcutaneous parts of rat's back and then suture it. The cross sections in the middle part of the samples were stained with hematoxylin and eosin (H&E) at 2 and 4 weeks after surgery to observe tissue infiltration.

Histological Analysis and Immunofluorescence: For histological analysis, regenerated nerves were dissected at 12 weeks post-surgery. H&E and toluidine blue (TB) staining were used to observe the overview of

regenerated nerve tissue of cross sections in the middle part of the samples. For immunofluorescence staining, the cross sections in the middle part of the regenerated nerve tissues were incubated with S-100 β and NF-200.

Animal Behavior Test: A walking track analysis was carried out to measure functional recovery of sciatic nerves at 4 and 12 weeks. Rats with their hind limbs stained with red ink were placed on the surface of a blank sheet of paper, and footprints were reported as rats moving. The values of toe spread length (TS), intermediary toe spread (IT) and paw length (PL) of both the experimental (E) and normal (N) legs were measured and finally the sciatic function index (SFI) was calculated using the following formula,^[55]

$$\text{SFI} = 13.3 \times \frac{E \times \text{IT} - N \times \text{IT}}{N} \times \text{IT} - 38.3 \times \frac{E \times \text{PL} - N \times \text{PL}}{N} \times \text{PL} + 109.5 \times \frac{E \times \text{TS} - N \times \text{TS}}{N} \times \text{TS} - 8.8 \quad (2)$$

Muscle Wet Weight and Histological Evaluation: For triceps weight analysis, the triceps surae muscle (TSM) was collected and weighed from both sides of each rat. The percentage of TSM weight was calculated as follows (3):

$$\text{TSM weight ratio (\%)} = \frac{\text{TSM (experimental leg)}}{\text{TSM (normal leg)}} \times 100 \quad (3)$$

TSMs were also sectioned for Masson's staining and the percentage of collagen was determined using Image J software.

Statistical Analysis: All data were presented as mean \pm standard deviation. Statistical analysis was carried out by one-way ANOVA followed by Tukey's test, and Student's *t*-test using GraphPad Prism software (version 9.0). $p < 0.05$ (*), $p < 0.01$ (**), and $p < 0.001$ (***) were statistically significant.

Supporting Information

Supporting Information is available from the Wiley Online Library or from the author.

Acknowledgements

J.S. and J.D. contributed equally to this work. This work was supported by Science and Technology Commission of Shanghai Municipality, China (20DZ2254900), National Key Research and Development Program of China (2021FYC2400800), Sino German Science Foundation Research Exchange Center, China (M-0263), and China Education Association for International Exchange (2022181). This project was also supported by Researchers Supporting Project Number (RSP2024R65), King Saud University, Riyadh, Saudi Arabia.

Conflict of Interest

The authors declare no conflict of interest.

Data Availability Statement

The data that support the findings of this study are available from the corresponding author upon reasonable request.

Keywords

conductive NGCs, electrospun nanofibers, peripheral nerve regeneration, shape memory

Received: March 27, 2024

Revised: May 9, 2024

Published online:

- [1] Y. Ma, H. Wang, Q. Wang, X. Cao, H. Gao, *Chem. Eng. J.* **2023**, *452*, 139424.
- [2] P. Zarrintaj, M. R. Saeb, S. Ramakrishna, M. Mozafari, *Curr. Opin. Cell Biol.* **2018**, *6*, 99.
- [3] Y. Qian, J. Song, X. Zhao, W. Chen, Y. Ouyang, W. Yuan, C. Fan, *Adv. Sci.* **2018**, *5*, 1700499.
- [4] T. Khan, R. Waseem, Z. Zehra, A. Aiman, P. Bhardwaj, J. Ansari, M. I. Hassan, A. Islam, *Pharmaceutics* **2022**, *14*, 2657.
- [5] F. Xiong, S. Wei, S. Wu, W. Jiang, B. Li, H. Xuan, Y. Xue, H. Yuan, *ACS Appl. Mater. Interfaces* **2023**, *15*, 41385.
- [6] R. Deng, Z. Luo, Z. Rao, Z. Lin, S. Chen, J. Zhou, Q. Zhu, X. Liu, Y. Bai, D. Quan, *Adv. Fiber Mater.* **2022**, *4*, 503.
- [7] T. J. Sill, H. A. von Recum, *Biomaterials* **2008**, *29*, 1989.
- [8] B. Gong, X. Zhang, A. A. Zahrani, W. Gao, G. Ma, L. Zhang, J. Xue, *Exploration* **2022**, *2*, 20210035.
- [9] Z. Chen, M. Guan, Y. Bian, X. Yin, M. E. N. Biosensing, B. E. Applications, *Biosensors* **2023**, *14*, 13.
- [10] J. Xie, M. R. MacEwan, A. G. Schwartz, Y. Xia, *Nanoscale* **2010**, *2*, 35.
- [11] D. Grinsell, C. P. Keating, *Biomed Res. Int.* **2014**, *2014*, 698256.
- [12] L. Zhang, R. Sun, B. Wang, Y. Lang, M.-W. Chang, *Int. J. Polym. Mater. Polym. Biomater.* **2023**, *1*, 661.
- [13] X. Hu, X. Wang, Y. Xu, L. Li, J. Liu, Y. He, Y. Zou, L. Yu, X. Qiu, J. Guo, *Adv. Healthcare Mater.* **2020**, *9*, 1901570.
- [14] J. Hu, D. Kai, H. Ye, L. Tian, X. Ding, S. Ramakrishna, X. J. Loh, *Mater. Sci. Eng., C* **2017**, *70*, 1089.
- [15] J. Wang, H. Xiong, T. Zhu, Y. Liu, H. Pan, C. Fan, X. Zhao, W. W. Lu, *ACS Nano* **2020**, *14*, 12579.
- [16] Q. Zhao, J. Wang, H. Cui, H. Chen, Y. Wang, X. Du, *Adv. Funct. Mater.* **2018**, *28*, 1801027.
- [17] M. Bao, X. Wang, H. Yuan, X. Lou, Q. Zhao, Y. Zhang, *J. Mater. Chem. B* **2016**, *4*, 5308.
- [18] H. R. El-Seedi, N. S. Said, N. Yosri, H. B. Hawash, D. M. El-Sherif, M. Abouzid, M. M. Abdel-Daim, M. Yaseen, H. Omar, Q. Shou, N. F. Attia, X. Zou, Z. Guo, S. A. M. Khalifa, *Heliyon* **2023**, *9*, 16228.
- [19] E. Mooney, J. N. Mackle, D. J. P. Blond, E. O'Ceirbhail, G. Shaw, W. J. Blau, F. P. Barry, V. Barron, J. M. Murphy, *Biomaterials* **2012**, *33*, 6132.
- [20] M. Biefeldt, K. Budde-Sagert, N. Weis, M. Buehning, S. Staehle, J. Zimmermann, N. Arbeiter, S. Mobini, M. U. González, H. Rebl, A. Uhrmacher, U. van Rienen, B. Nebe, *J. Biol. Eng.* **2023**, *17*, 71.
- [21] Y. Wu, L. Wang, B. Guo, Y. Shao, P. X. Ma, *Biomaterials* **2016**, *87*, 18.
- [22] R. Liu, X. Huang, X. Wang, X. Peng, S. Zhang, Y. Liu, D. Yang, Y. Min, *Appl. Surf. Sci.* **2021**, *560*, 149965.
- [23] P. Zarrintaj, E. Zangene, S. Manouchehri, L. M. Amirabad, N. Baheiraei, M. R. Hadjighasem, M. Farokhi, M. R. Ganjali, B. W. Walker, M. R. Saeb, M. Mozafari, S. Thomas, N. Annabi, *Appl. Mater. Today* **2020**, *20*, 100784.
- [24] Y. Han, M. Sun, X. Lu, K. Xu, M. Yu, H. Yang, J. Yin, *Composites, Part B* **2024**, *273*, 111241.
- [25] A. J. Ryan, C. J. Kearney, N. Shen, U. Khan, A. G. Kelly, C. Probst, E. Brauchle, S. Bicca, C. D. Garciaarena, V. Vega-Mayoral, P. Loskill, S. W. Kerrigan, D. J. Kelly, K. Schenke-Layland, J. N. Coleman, F. J. O'Brien, *Adv. Mater.* **2018**, *30*, 1706442.
- [26] V. V. Neklyudov, N. R. Khafizov, I. A. Sedov, A. M. Dimiev, *Phys. Chem. Chem. Phys.* **2017**, *19*, 17000.
- [27] Y. Wang, Y. Chen, S. D. Lacey, L. Xu, H. Xie, T. Li, V. A. Danner, L. Hu, *Materials* **2018**, *21*, 186.
- [28] H. A. Strobel, E. L. Calamari, A. Beliveau, A. Jain, M. W. Rolle, *J. Biomed. Mater. Res., Part B* **2017**, *106*, 817.

- [29] M. M. Abdel-Mottaleb, A. Mohamed, S. A. Karim, T. A. Osman, A. Khattab, *Mech. Adv. Mater. Struct.* **2018**, *27*, 346.
- [30] J. Wang, Y. Cheng, L. Chen, T. Zhu, K. Ye, C. Jia, H. Wang, M. Zhu, C. Fan, X. Mo, *Acta Biomater.* **2019**, *84*, 98.
- [31] Q. Li, X. Qin, Y. Luo, W. Lu, G. Chang, A. M. Asiri, A. O. Al-Youbi, X. Sun, *Electrochim. Acta* **2012**, *83*, 283.
- [32] J. Zhang, H. Yang, G. Shen, P. Cheng, J. Zhang, S. Guo, *Chem. Commun.* **2010**, *46*, 1112.
- [33] W. Fu, Z. Liu, B. Feng, R. Hu, X. He, H. Wang, M. Yin, H. Huang, H. Zhang, W. Wang, *Int. J. Nanomed.* **2014**, *2014*, 2335.
- [34] C. S. Taylor, J. Barnes, M. Prasad Koduri, S. Haq, D. A. Gregory, I. Roy, R. A. D'Sa, J. Curran, J. W. Haycock, *Macromol. Biosci.* **2023**, *23*, 2300226.
- [35] L. Luo, Y. He, L. Jin, Y. Zhang, F. P. Guastaldi, A. A. Albashari, F. Hu, X. Wang, L. Wang, J. Xiao, L. Li, J. Wang, A. Higuchi, Q. Ye, *Bioact. Mater.* **2021**, *6*, 638.
- [36] M. Anderson, N. B. Shelke, O. S. Manoukian, X. Yu, L. D. McCullough, S. G. Kumbar, *Crit. Rev. Biomed. Eng.* **2015**, *43*, 131.
- [37] L. Yao, G. C. de Ruiter, H. Wang, A. M. Knight, R. J. Spinner, M. J. Yaszemski, A. J. Windebank, A. Pandit, *Biomaterials* **2010**, *31*, 5789.
- [38] Q. Dong, X. Yang, X. Liang, J. Liu, B. Wang, Y. Zhao, C. Huselstein, X. Feng, Z. Tong, Y. Chen, *ACS Appl. Mater. Interfaces* **2023**, *15*, 24120.
- [39] Y. Hu, Z. Chen, H. Wang, J. Guo, J. Cai, X. Chen, H. Wei, J. Qi, Q. Wang, H. Liu, Y. Zhao, R. Chai, *ACS Nano* **2022**, *16*, 1868.
- [40] C. Cai, H. Zhu, Y. Chen, C. Chen, H. Li, Z. Yang, H. Liu, *Appl. Mater. Today* **2022**, *27*, 101491.
- [41] L. A. L. Tang, W. C. Lee, H. Shi, E. Y. L. Wong, A. Sadovoy, S. Gorelik, J. Hobley, C. T. Lim, K. P. Loh, *Small* **2011**, *8*, 423.
- [42] Y. Chen, Y. Zheng, Y.-N. Zhao, P. Wu, Z.-Y. Zhao, F.-X. Chen, A. Xiao, Z.-Y. Yue, X.-W. Han, *Neural Regen. Res.* **2023**, *18*, 207.
- [43] J. Wang, Y. Cheng, H. Wang, Y. Wang, K. Zhang, C. Fan, H. Wang, X. Mo, *Acta Biomater.* **2020**, *117*, 180.
- [44] N. G. Shang, P. Papakonstantinou, M. McMullan, M. Chu, A. Stamboulis, A. Potenza, S. S. Dhesi, H. Marchetto, *Adv. Funct. Mater.* **2008**, *18*, 3506.
- [45] Y. Zhang, S. F. Ali, E. Dervishi, Y. Xu, Z. Li, D. Casciano, A. S. Biris, *ACS Nano* **2010**, *4*, 3181.
- [46] X. Zhao, P. Li, B. Guo, P. X. Ma, *Acta Biomater.* **2015**, *26*, 236.
- [47] J. Park, J. Jeon, B. Kim, M. S. Lee, S. Park, J. Lim, J. Yi, H. Lee, H. S. Yang, J. Y. Lee, *Adv. Funct. Mater.* **2020**, *30*, 2003759.
- [48] A. Veith, X. Li, H. Modi, A. Abbaspour, L. Luan, C. Xie, A. B. Baker, *Biomaterials* **2021**, *275*, 120924.
- [49] T. Zhu, H. Gu, H. Zhang, H. Wang, H. Xia, X. Mo, J. Wu, *Acta Biomater.* **2021**, *119*, 211.
- [50] F. Mathot, N. Rbia, A. T. Bishop, S. E. R. Hovius, A. Y. Shin, *Microsurgery* **2020**, *40*, 585.
- [51] M. Caillaud, L. Richard, J. M. Vallat, A. Desmoulière, F. Billet, *Neural Regen. Res.* **2019**, *14*, 24.
- [52] Y. Zhao, Y. Liu, C. Lu, D. Sun, S. Kang, X. Wang, L. Lu, *Int. J. Nanomed.* **2024**, *19*, 2341.
- [53] Z. Yuan, D. Sheng, L. Jiang, M. Shafiq, A. U. R. Khan, R. Hashim, Y. Chen, B. Li, X. Xie, J. Chen, Y. Morsi, X. Mo, S. Chen, *Acta Biomater.* **2022**, *140*, 233.
- [54] J. Wang, H. Wang, X. Mo, H. Wang, *Adv. Mater.* **2020**, *32*, 2004555.
- [55] L. de Medinaceli, W. J. Freed, R. J. Wyatt, *Exp. Neurol.* **1982**, *77*, 634.